POLITECNICO DI TORINO
Repository ISTITUZIONALE

A shape sensing methodology for beams with generic cross-sections: Application to airfoil beams

Original
A shape sensing methodology for beams with generic cross-sections: Application to airfoil beams / Roy, R., Gherlone, M., Surace, C.. - In: AEROSPACE SCIENCE AND TECHNOLOGY. - ISSN 1270-9638. - STAMPA. - 110:(2021), pp. 1-10. [10.1016/j.ast.2020.106484]

Availability:
This version is available at: 11583/2869407 since: 2021-02-02T11:28:35Z

Publisher:
Elsevier Masson s.r.l.

Published
DOI:10.1016/j.ast.2020.106484

Terms of use:

This article is made available under terms and conditions as specified in the corresponding bibliographic description in the repository

Publisher copyright

(Article begins on next page)

19 November 2026

A Shape Sensing Methodology for Beams with Generic Cross-Sections: Application to Airfoil Beams

Rinto Roy[a,*], Marco Gherlone[a], Cecilia Surace[b]

[a] *Department of Mechanical & Aerospace Engineering,Politecnico di Torino, Corso Duca degli Abruzzi, 10129 Torino, Italy*
[b] *Department of Structural, Geotechnical and Building Engineering,Politecnico di Torino, Corso Duca degli Abruzzi, 10129 Torino, Italy*

Abstract

This work presents a shape sensing method capable of handling some geometrical complexities commonly observed in aerospace structures. The method presented is based on the one-dimensional inverse Finite Element Method (1D-iFEM), which is capable of accurately reconstructing structural displacements of beam structures using surface strain measurements. The effects of cross-sectional variation in shear strains due to transverse or torsional loads for any general beam profile is accounted for in this 1D-iFEM formulation. The introduction of these effects allows the use of iFEM for the shape sensing of solid or thin-walled prismatic beams with any general beam profile. The performance of the new method is demonstrated through some example

*Corresponding author
Email address: rinto.roy@polito.it (Rinto Roy)

problems of prismatic beams under various static loading scenarios.

Keywords: Timoshenko Beam, Shape Sensing, Structural Health Monitoring

1. Introduction

For a mechanical structure, obtaining the strain field given a continuous displacement field is a well-defined problem. Theoretically, it is governed by the strain-displacement relationships, and one example of its numerical application is observed when using the Finite Element Method (FEM). However, the inverse problem of obtaining the displacement field using continuous or discrete strain data is ill-defined and suffers from the issues of existence and uniqueness of a solution. However, it is a problem of considerable significance for various practical aerospace applications.

One field of application is for Structural Health Monitoring (SHM), where the mechanical quantity measured by sensors embedded in the structure is often strain or acceleration. In this context, a full-scale reconstruction of the displacement and, subsequently, stress fields can be used to calculate damage indexes based on stress concentration or displacement curvature [1, 2, 3]. Such damage indexes can be used to identify the presence of damage in the structure. Another application is for morphing structures where knowledge

of the structural shape is critical, but often, the displacement field cannot be measured directly. Real-time displacement reconstruction using strain sensor data can be used as a feedback component when designing a control system for the active control of the shape of the structure [4, 5]. In all these cases, techniques that can reconstruct the displacement field, using discrete or continuous strain data measured on the surface of the structure, are called shape sensing techniques [6, 7, 8, 9, 10].

The inverse Finite Element Method (iFEM) is one such shape sensing technique, developed separately for 2D plate and shell structures[11, 12] and 1D beam structures [13]. For the shape sensing of any general 3D beam or frame structure, the 1D iFEM methodology is used. It is based on minimizing a least-square functional defined as the difference between the theoretical and experimental sectional strain measures. The sectional strain measures are defined based on the Timoshenko beam theory and correspond to the axial, bending, transverse shear, and torsional strains experienced by any beam section. The results of the iFEM reconstruction are computationally efficient and robust in the presence of measurement noise. It can handle structures subjected to both static and dynamic loading [13] and in the geometrically linear and non-linear deformation regimes as well [14]. As the methodology is

independent of the structure's material properties and loading conditions, it is suitable for various SHM problems. Application of iFEM for SHM has been demonstrated for simple 1D structures using Fibre-Optic sensors [15] and simple plate structures with embedded cracks, using strain sensor grids [16, 3]. As 1D iFEM accuracy is dependent on the location and orientation of the strain sensors on the structure, various optimal sensor placement techniques have also been developed. Multi-parameter optimization problems solved using the Particle Swarm Optimization (PSO) algorithm [17, 18] can be used to identify optimal sensor positions that minimize the effect of experimental noise and maximize the accuracy of the iFEM reconstruction.

The 1D-iFEM was initially proposed for solving problems involving prismatic beams with simple circular or rectangular profiles [13, 19]. While efforts have focused on expanding the method for more complex structures, such as using an iso-geometric analysis for handling non-prismatic beams[20], the 1D-iFEM formulation still produces inaccurate results when handling beams with complex cross-sections, such as an airfoil. An initial effort to generalize the 1D formulation for any general beam cross-section was made by capturing the dependence of transverse shear strain on the shape of the beam cross-section [21]. However, the applicability of the method is con-

strained to those structures satisfying the assumptions of the formulation. Expanding the methodology to more practical aerospace structures, such as an aircraft wing-box, requires further development of the formulation. The method should be able to handle effects such as torsional deformation, cross-sectional warping, cases of non-prismatic and tapered beams, and the effects of additional stiffening members such as ribs and spars. This paper presents a gradual step in this direction by introducing some of these features into the existing 1D iFEM formulation.

The paper begins with the theoretical description of the 1D-iFEM for beams. The improvements proposed to account for shear and torsional loading are described in section 2. Section 3 gives a brief review of some numerical techniques which can be used for computing the transverse shear strain variation due to shear and torsional loading for any general beam profile. Section 4 describes an optimal sensor placement technique and presents the results of some example problems of prismatic beams under various static loading scenarios. Finally, section 5 concludes with the paper's main achievements and presents potential areas for future work.

2. Theoretical Formulation

The theoretical formulation of the 1D and 2D iFEM for beam, plate, and shell structures has been discussed extensively in previous papers by Gherlone et al.[13, 19] and Tessler et al. [11]. The readers are encouraged to go through these to get a detailed explanation of the technique. This section briefly explains the iFEM formulation for 1D structures and the efforts to generalize the formulation for prismatic beams with any general cross-sectional profile.

2.1. inverse Finite Element Method for Beams

The 1D-iFEM is based on the Timoshenko beam theory, where the displacement field of the beam can be defined using the six kinematic variables, $\{u, v, w, \theta_x, \theta_y, \theta_z\}$ (see Figure 1) as,

$$\begin{aligned} u_x(x,y,z) &= u(x) + z\theta_y(x) - y\theta_z(x) \\ u_y(x,y,z) &= v(x) - z\theta_x(x) \\ u_z(x,y,z) &= w(x) + y\theta_x(x) \end{aligned} \tag{1}$$

Based on the small-strain hypothesis, the axial and transverse shear strain components on any section of the beam can be described as,

$$\epsilon_x(x,y,z) = e_1(x) + ze_2(x) + ye_3(x)$$

$$\gamma_{xz}(x,y,z) = e_4(x) + ye_6(x) \tag{2}$$

$$\gamma_{xy}(x,y,z) = e_5(x) - ze_6(x)$$

where $e_i, (i = 1, ..., 6)$ are the sectional strain measures of the beam. These strain measures represent the axial, bending, transverse shear, and torsional strains and can be defined in terms of the six kinematic variables as,

$$e_1(x) = u_{,x}(x) \quad e_2(x) = \theta_{y,x}(x) \quad e_3(x) = -\theta_{z,x}(x) \tag{3}$$

$$e_4(x) = w_{,x} + \theta_y(x) \quad e_5(x) = v_{,x} - \theta_z(x) \quad e_6(x) = \theta_{x,x}(x)$$

The displacement reconstruction is performed by discretizing the beam into a set of inverse elements and interpolating the kinematic variables, and as a consequence the sectional strain measures, using element shape functions. For each inverse element of the beam, e, and each sectional strain measure, k, the functional ϕ_k^e can be defined as the least square error between the

theoretical and the experimental value of that strain measure,

$$\phi_k^e = \frac{L^e}{n} \sum_{i=1}^{n} [e_k(x_i) - e_k^{exp,i}]^2 \quad (k = 1, ..., 6) \tag{4}$$

where L^e is the element length, and n is the number of axial locations in an element where the experimental strain measures have been calculated. The experimental sectional strain measures are calculated using linear strain measurements made on the outer surface of the beam. The element functional ϕ^e can be written as the sum of the individual functionals, ϕ_k^e, multiplied by suitable weighing coefficients, $w_i, (i = 1, ..., 6)$, which are calculated using the area, second moments of inertia, and polar moment of inertia of the beam cross-section [13].

$$\phi^e = \sum_{k=1}^{6} w_k^e \phi_k^e \tag{5}$$

Individual contributions from all the elements are assembled as in the direct FEM, and the final functional, ϕ, is minimized with respect to the unknown nodal degrees of freedom to get a set of linear algebraic equations. These equations can be solved to obtain the nodal displacements of the beam.

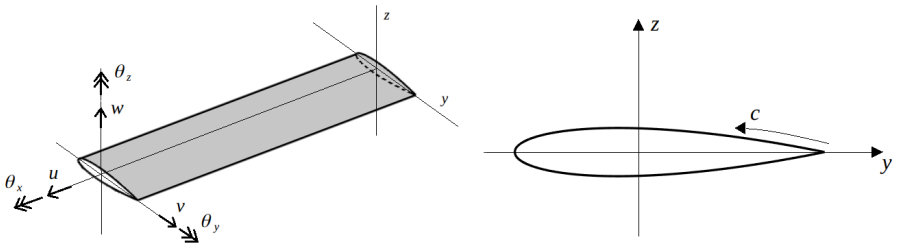


Figure 1: Sign conventions used for the six kinematic variables of the beam (left); NACA 0016 airfoil profile with the parameter c indicating the distance along the perimeter (right)

2.2. Estimating Strain Measures

To implement the iFEM procedure, the six sectional strain measures of the beam have to be calculated using experimental linear strain measurements made on the surface of the beam. This calculation can be done by formulating a set of equations relating these two quantities. The calculation of the strain measures for prismatic beams with simple profiles has been discussed previously by Gherlone et al. [13, 19]. This formulation was expanded by Roy et al. [21] to accommodate prismatic beams with any general cross-sectional profile, with specific examples of symmetric airfoil profiles. However, the previous work was not successful in accurately accounting for the distribution of transverse shear strains due to torsion. The present work handles this limitation and provides a more detailed explanation of the entire procedure.

Assuming a prismatic beam with any arbitrary solid cross-section sub-

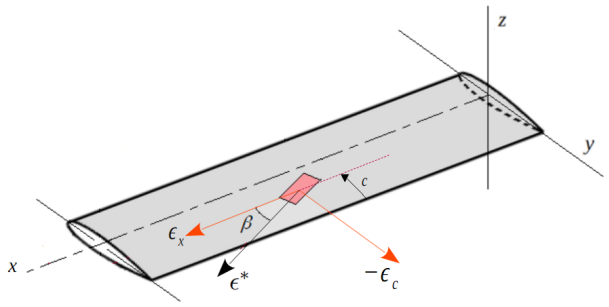


Figure 2: Strain gauge placed on the surface of the beam, oriented at an angle β with respect to the axis of the beam

jected to a generalized tip load consisting of axial, transverse and torsional loads. The magnitude of strain, ϵ^*, measured by a linear strain gauge placed on the outer surface of the beam and oriented at an angle, β, with respect to the beam-axis (see Figure 2) can be written as a function of the axial strain,ϵ_x, tangential strain,ϵ_c, and tangential shear strain, γ_{xc}, on the perimeter of the beam section. Using a suitable strain-tensor transformation, it can be defined as[13],

$$\epsilon^*(x, c, \beta) = \epsilon_x(x, c)cos^2\beta + \epsilon_c(x, c)sin^2\beta + \gamma_{xc}(x, c)cos\beta sin\beta \qquad (6)$$

where c represents the distance along the perimeter from the trailing edge for either solid or thin-walled beam sections (see Figure 1). Equation 6 can

be further simplified as [13],

$$\epsilon^*(x, c, \beta) = \epsilon_x(x, c)(cos^2\beta - \nu sin^2\beta) + \gamma_{xc}(x, c)cos\beta sin\beta \tag{7}$$

Here the axial strain, $\epsilon_x(x, c)$, and tangential shear strain, $\gamma_{xc}(x, c)$, should be represented in terms of the strain measures. Using Equation 2, the distribution of ϵ_x along the perimeter of the beam can be written as,

$$\epsilon_x(x, c) = e_1(x) + e_2(x)z(c) + e_3(x)y(c) \tag{8}$$

Variation of γ_{xc} along the perimeter can be represented as a superposition of strains due to transverse and torsional loads. Under a transverse or torsional load, the shear strain at any section is not constant but is a function of the parameter c. The tangential shear strain variation due to a transverse load along the z-axis can be represented with the help of the shear strain variation function, $f_1(c)$, and the tangential shear strain maximum, $\gamma^z_{xc,max}$, which represents the amplitude of the variation. Similarly, the tangential shear strain variation due to a transverse load along the y-axis can be represented with the help of the shear strain variation function, $f_2(c)$, and the tangential shear strain maximum, $\gamma^y_{xc,max}$, which represents the amplitude of

the variation. The overall tangential shear strain variation due to the two transverse loads will be the sum of these two contributions.

For the case of a torsional load, it is assumed that the effect of warping is negligible. Hence, the tangential shear strain variation for a beam due to a torsional load at the tip is represented using the torsional strain measure, e_6, and the function $f_3(c)$, which indicates the variation of tangential shear strain associated with a unit rate of twist ($e_6 = 1$). Hence the overall variation of γ_{xc} along the perimeter of the beam can be written as,

$$\gamma_{xc}(x, c) = \gamma^z_{xc,max}(x) f_1(c) + \gamma^y_{xc,max}(x) f_2(c) + e_6(x) f_3(c) \tag{9}$$

The quantities $\{\gamma^z_{xc,max}, \gamma^y_{xc,max}, e_6\}$ are proportional to the magnitudes of the loads along the z and y-axes and torsional load along the x-axis respectively. For a 3D beam, the transverse shear strain varies over the cross-section and is in contrast to the Timoshenko beam theory that proposes a constant transverse shear strain for any cross-section. Therefore, for implementing the 1D-iFEM, $\{\gamma^z_{xc,max}, \gamma^y_{xc,max}\}$, which are measured experimentally have to be related to the sectional strain measures, $\{e_4, e_5\}$, which are based on the Timoshenko beam theory.

For the case of a cantilevered prismatic beam with a tip load, F_z, applied

along the z-axis, this can be done by equating the shear strain energy per unit length at the mid-beam cross-section (to avoid end-effects) for a 3D beam, with a similar case for a Timoshenko beam. Under the Timoshenko beam theory, the shear strain energy per unit length will be the same in any beam section. For the present case, the shear strain energy per unit length for the Timoshenko beam,ϕ_{SE}^{Tim}, can be defined as,

$$\phi_{SE}^{Tim} = \frac{F_z^2}{2AG} \tag{10}$$

where A indicates the area of the beam cross-section, and G represents the shear modulus of the beam material. The two shear strain energies can be equated using a coefficient,k_{tz}, which is the classical shear correction factor, and is defined as the ratio between the two quantities,

$$k_{tz} = \frac{\phi_{SE}^{Tim}}{\phi_{SE}^{FE}} = \frac{F_z^2}{2AG\phi_{SE}^{FE}} = \frac{F_z/GA}{e_4} \tag{11}$$

where ϕ_{SE}^{FE} is the shear strain energy calculated using a high-fidelity 3D FE analysis or any equivalent highly accurate approach. The coefficient, k_{ty}, can be calculated similarly by calculating ϕ_{SE}^{Tim} and ϕ_{SE}^{FE} for a load applied along

the y-axis.

$$k_{ty} = \frac{\phi_{SE}^{Tim}}{\phi_{SE}^{FE}} = \frac{F_y^2}{2AG\phi_{SE}^{FE}} = \frac{F_y/GA}{e_5} \tag{12}$$

Now, $\{e_4, e_5\}$ can be related to $\{\gamma_{xc,max}^z, \gamma_{xc,max}^y\}$ using the coefficients, $\{k_{\epsilon y}, k_{\epsilon z}\}$, which are defined as the ratio between the two,

$$k_{\epsilon z} = \frac{e_4}{\gamma_{xc,max}^z} = \frac{F_z/GA}{k_{tz}\gamma_{xc,max}^z} \quad , \quad k_{\epsilon y} = \frac{e_5}{\gamma_{xc,max}^y} = \frac{F_y/GA}{k_{ty}\gamma_{xc,max}^y} \tag{13}$$

The coefficients, $\{k_{ty}, k_{\epsilon y}, k_{tz}, k_{\epsilon z}\}$, are purely functions of the shape of the beam section. The tangential shear strain along the perimeter of the beam can be written in terms of the shear coefficients as,

$$\gamma_{xc}(x, c) = \frac{1}{k_{\epsilon z}} e_4(x) f_1(c) + \frac{1}{k_{\epsilon y}} e_5(x) f_2(c) + e_6(x) f_3(c) \tag{14}$$

Finally, the experimentally measured surface strains can be written as a function of the sectional strain measures by substituting Equations 8 and 14 into Equation 7,

$$\epsilon^*(x,c,\beta) = \Big(e_1(x) + e_2(x)z(c) + e_3(x)y(c)\Big)[cos^2\beta - \nu sin^2\beta] + \Big(\frac{1}{k_{\epsilon z}}e_4(x)f_1(c) + \frac{1}{k_{\epsilon y}}e_5(x)f_2(c) + e_6(x)f_3(c)\Big)cos\beta sin\beta \quad (15)$$

As Equation 15 is a linear algebraic equation with six unknowns, at least six experimental strain measurements are required at a beam section for solving the equation.

2.3. Calculating coefficients and functions

A more detailed explanation of the procedure used for calculating the functions, $\{f_1, f_2, f_3\}$, and coefficients, $\{k_{ty}, k_{\epsilon y}, k_{tz}, k_{\epsilon z}\}$, is provided for the case of a prismatic beam with a solid NACA 0016 airfoil profile. The beam considered has a length of 20 m and a chord length of 1m. Results from a high fidelity 3D FE model of the beam is used for the calculations. The beam model is meshed in ABAQUS using solid C3D8R elements, with 8490 elements used per cross-section and 100 elements used along the beam length to ensure convergent results (see Table 1). An example of the meshed beam cross-section is shown in Figure 3.

For calculating the coefficients and functions for a load along the z-axis,

Table 1: Element discretization details of the FE model used in the numerical procedure: for the case of solid beam models

	Elements used		
Solid Profile	Per cross-section	Along beam length	Total
NACA 0016	8490	100	849000
NACA 6516	8710	100	871000

Table 2: Element discretization details of the FE model used in the numerical procedure: for the case of thin-walled beam models (thickness=5mm)

	Elements used		
Thin-walled Profile	Per cross-section	Along beam length	Total
NACA 0016	4828	150	642124
NACA 6516	4495	150	674250

196 the FE beam model, clamped at one end, is subject to a unit tip load along the z-axis. The FE results are used to calculate the shear strain energy per 198 unit length for any beam cross-section. Undesired contributions due to end effects caused by beam clamping and loading are avoided by considering the 200 beam's mid-way cross-section.

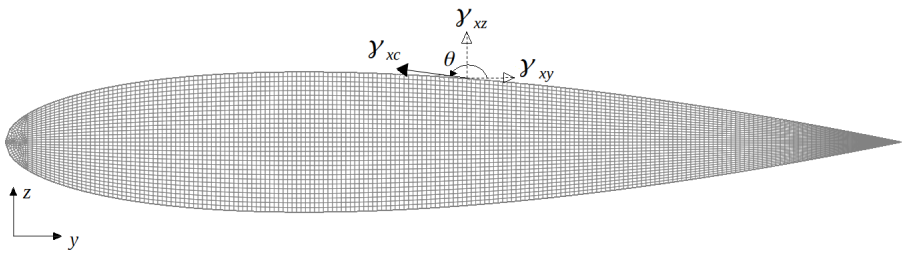


Figure 3: FE mesh of the beam cross-section for the solid beam model with a NACA 0016 airfoil profile

As the beam is meshed using solid elements, it is assumed that the strain and stress variations within each element is a constant and has a value equal to that at the centroid of the element.Now that the stress and strain variation is independent of the element length, the shear strain energy per unit length for each element is calculated as the product of the shear stress and shear strain integrated over the projected element area in the mid-beam cross-section. The total shear strain energy per unit length can be found as the sum of the shear strain energies of each element of the cross-section,

$$\phi_{SE}^{FE} = \frac{1}{2}\int_A (\tau_{xz}^{FE}\gamma_{xz}^{FE} + \tau_{xy}^{FE}\gamma_{xy}^{FE})dA = \frac{1}{2}\sum_{i=1}^{N_{elem}} (\tau_{xz}\gamma_{xz} + \tau_{xy}\gamma_{xy})_i A_i^e \qquad (16)$$

where, A_i^e indicates the projected area of each element of the cross-section and the transverse shear strains and stresses, $\{\tau_{xz}, \gamma_{xz}, \tau_{xy}, \gamma_{xy}\}_i$ are calculated at the centroid of each element of the cross-section. The variation of tangential shear strain, γ_{xc}, along the perimeter can be calculated as a combination of the two transverse shear strain components along the perimeter. For any node lying on the perimeter of the beam section, γ_{xc} on that node can be

calculated as (see Figure 3),

$$\gamma_{xc}(c) = \gamma_{xy}(c)\cos(\theta(c)) + \gamma_{xz}(c)\sin(\theta(c)) \tag{17}$$

where, angle θ represents the angle between the horizontal, y-axis, and the tangent to the cross-section at that node. Iterating through all the nodes along the perimeter, the variation of γ_{xc} and the corresponding tangential shear strain maxima,$\gamma^z_{xc,max}$, can be calculated for a unit tip load along the z-axis. Using the shear strain energy and the tangential shear strain maxima obtained, the shear coefficients, $\{k_{tz}, k_{\epsilon z}\}$ can be calculated using Equations 11 and 13. The variation function, $f_1(c)$, is obtained by calculating the tangential shear strain variation using Equation 17 and representing the variation using a suitable Fourier series or polynomial function.

A similar process can be used to obtain the shear coefficients, $\{k_{ty}, k_{\epsilon y}\}$ and variation function, $f_2(c)$, using a FEM beam model with a unit tip load applied along the y-axis.

To obtain the variation function, $f_3(c)$, a beam model with a unit torsional strain applied at the beam tip is used and Equation 17 is used for calculating the tangential shear strain variation. For the example case of a solid prismatic beam with a NACA 0016 airfoil profile, the shear coefficients calculated using

Table 3: Shear Coefficients for some common airfoil profiles

Beam Profile	Type	k_{ty}	k_{tz}	$k_{\epsilon y}$	$k_{\epsilon z}$
NACA 0016	Solid	0.91	0.31	0.84	1.24
NACA 0016	Thin-walled (t=5mm)	0.75	0.03	0.85	3.93
NACA 6516	Solid	1.01	0.28	0.81	1.15
NACA 6516	Thin-walled (t=5mm)	0.83	0.03	0.73	3.06

the above procedure is provided in Table 3 and the variation functions are represented using a suitable Fourier series expansions as,

$$f_1(c) = \cos(\frac{3}{2}\pi\frac{c}{P}) \quad , \quad f_2(c) = \sin(\pi\frac{c}{P}) \tag{18}$$

$$f_3(c) = 0.9\sin(2.3c + 0.4) + 0.24\sin(12.6c - 1.6)$$

where, P, indicates the half perimeter distance of the cross-section. A similar procedure was used to calculate the shear coefficients for some alternative solid and thin-walled, symmetric, and cambered airfoil profiles. The details of the FE mesh used for these beam profiles are provided in Tables 1 and 2, and the coefficients calculated using the numerical procedure are shown in Table 3.

3. Numerical methods for calculating coefficients and functions

The calculation of the functions, $\{f_1, f_2, f_3\}$, and coefficients, $\{k_{\epsilon y}, k_{\epsilon z}\}$, for any arbitrary beam profile is essential for shape reconstruction based on the iFEM methodology described above. As these functions and coefficients are dependent on the beam profile, it is necessary to calculate them before implementation. A possible procedure was demonstrated in detail in the previous section, where a high fidelity 3D FE model of a beam with the desired profile under different loading scenarios was used. The drawbacks of using this procedure are that the results are obtained at a high computational cost due to the high fidelity mesh used and require an iterative exercise to simulate each beam profile under different loading scenarios. In this context, it would be useful to investigate alternative methods that would provide accurate analytical or numerical solutions at a lower computational cost.

The analytical solution of transverse shear strain for the bending or torsion of a cantilevered prismatic beam requires a solution based on the theory of elasticity. A solution for the torsion problem can be obtained using Saint-Venant's Semi-Inverse Method, where the axial displacement is considered a function of the warping function, $\psi(y, z)$. This problem can be solved by writing the warping function in terms of a stress function,$\Phi(y, z)$, satisfying

the Poisson's equation,

$$\Phi_{,yy} + \Phi_{,zz} = -2G\theta_{x,x} \tag{19}$$

where G is the shear modulus of the beam material. For solving the bending problem, the Semi-Inverse Method can be used again by making certain assumptions regarding the stress distribution across the beam. It can also be solved by representing the shear stresses using a suitable stress function, which satisfies the equilibrium equations, boundary conditions, and compatibility conditions. Closed-form solutions for Saint-Venant's bending and torsion problems exist only for a few simple cross-sections like a circle or rectangle [22]. The difficulties of finding an analytical solution can be avoided by considering a few simple numerical and semi-analytical methods. Some of these methods are discussed below.

Even though analytical solutions for the torsion problem of Equation 19 exists for simple cross-sections, it is not easy to find an exact solution for a general class of airfoil profiles. However, it is possible to obtain solutions for certain specific airfoil shapes using a specific definition of the stress function, which satisfies Equation 19, like a specific family of airfoils. This approach is described by Wang [23], where the stress function, is defined using specific

terms of a power series as,

$$\Phi = G\theta_{x,x}\Big(-\frac{y^2+z^2}{2} + a_0 + a_2(y^2-z^2) + a_4(y^4 - 6y^2z^2 + z^4)\Big) \qquad (20)$$

Here the values of the coefficients a_0, a_2, and a_4 are chosen such that the stress function satisfies Equation 19. They also define the boundary profile where, the stress function should be a constant ($\Phi = const = 0$). Values for the coefficients are chosen such that the boundary profile represents a family of airfoils. The limitation is that the closed-form torsion solutions are only available for some classes of symmetric airfoils. This method can only be used for the torsion problem, and hence only the function, f_3, can be calculated. Nonetheless, it does offer the ease of using a direct analytical solution for the iFEM procedure.

As discussed above, representation in terms of a power series is a powerful tool for solving such problems. Kosmatka [24] describes another approach for a prismatic beam under any general loading scenario. The overall bending and torsional warping function,ψ, is defined using a double power series

represented in terms of the coordinates of the beam profile,

$$\psi(y,z) = \sum_{m=0}^{\infty}\sum_{n=0}^{\infty} C_{mn} y^m z^n \tag{21}$$

Here the overall warping function can be assumed to be a linear combination of warping contributions due to beam bending and torsion. The coefficients, C_{mn}, are calculated using the principle of minimum potential energy, which is subsequently simplified to get a set of variationally defined linear algebraic equations. This procedure can be implemented numerically by discretizing the beam area using a series of triangular elements and solving the equations for each element. As it is used for solving the bending and torsion problems, all three functions, $\{f_1, f_2, f_3\}$, and coefficients can be calculated using this method. The advantage of this method is that it is capable of handling any general beam cross-section effectively.

As the aerospace domain is primarily concerned with thin-walled beam sections, the assumption that the shell thickness tends to zero can be used for obtaining useful, practical results regarding the transverse shear strain variation. Based on the above assumption, the Jourawski formula [25] offers a way of calculating the transverse shear variation functions,$\{f_1, f_2\}$, for closed thin-walled beam profiles, as a function of the length along the perimeter.

It can only be applied for transverse loading scenarios where the beam undergoes torsion-less bending. Hence, the function, f_3, cannot be computed. It can be applied to relatively simple sections, such as a thin-walled airfoil, or more complicated profiles such a thin-walled airfoil with a single or multiple supporting spar structures. The results, however, are constrained by the initial assumptions made. As wall thickness is a crucial assumption for thin-walled beams, more accurate solutions will be achieved when the wall thickness is low.

Further simplifications can be made for solving the torsional problem in the case of some thin-walled sections. Given the assumption that wall thickness tends to zero ($t \to 0$), the shear strain along the thickness can be considered uniform with a value equal to that along the center-line of the section thickness [25]. In such a scenario, it can be shown that the product of tangential shear strain along the section wall, $e_6(x)f_3(c)$, and the wall thickness, $t(c)$, is a constant. Hence, for a section with a constant wall thickness, the tangential shear strain variation, $f_3(c)$, is a constant with respect to the parameter, c.

The methods presented here summarize some analytical and numerical techniques explored by the authors for applying the iFEM for any complex

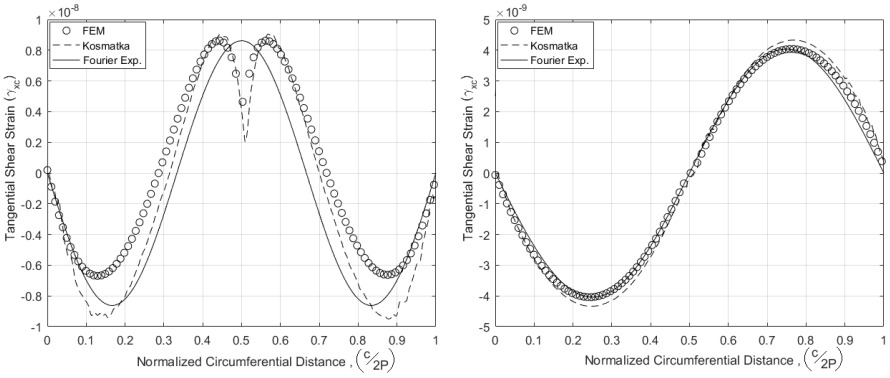


Figure 4: Comparison plot of the shear variation functions for a solid NACA 0016 airfoil profile, calculated based on different numerical methods: $f_1(c)$ due to a transverse load along the z-axis (left), $f_2(c)$ due to a transverse load along the y-axis (right)

beam profile. The list is by no means exhaustive, and more suitable methodologies might be available in the literature. For the case of a solid prismatic beam with a NACA 0016 airfoil profile, the three functions obtained using FE results, the approaches of Wang [23] and Kosmatka [24] and Fourier series approximations of Equation 18 are compared and plotted in Figures 4 and 5. Apart from the Fourier series approximations, the other approaches provide similar results. Similar results are also observed for beams with different profiles considered in Table 3. The shear coefficients can also be evaluated using the different approaches with similar results.

For these reasons, the FE approach is used to calculate the shear coefficients (Table 3), and these results will be used for the example problems described in Section 4. For calculating the functions $\{f_1, f_2, f_3\}$, a combination

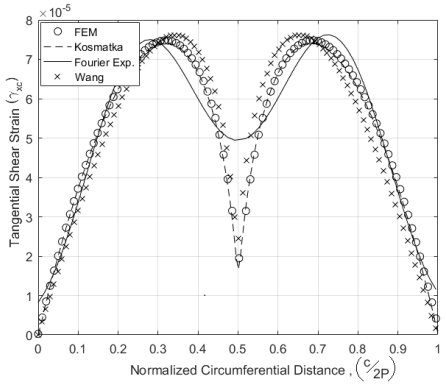


Figure 5: Comparison plot of the shear variation functions for a solid NACA 0016 airfoil profile, calculated based on different numerical methods: $f_3(c)$ due to a torsional load along the x-axis

of various methods are used. This is because the FE results do not provide a direct analytical expression, but a suitable Fourier series approximation has to be used to fit the data, leading to potential errors. Therefore, for all solid beam problems, functions $\{f_1, f_2\}$, are computed using the method of Kosmatka [24] and the torsion function,f_3, using the method of Wang [23]. For thin-walled beam problems, the Jourawski formula is used for computing functions,$\{f_1, f_2\}$, and a constant shear strain variation is used for the function,f_3, based on FE results. As described above, no one method is used for all problems. Depending on the beam cross-section, the method that offers the greatest ease in application, without loss of accuracy, is used in the iFEM formulation.

4. Application Problems

The performance of the formulation is tested through different example problems of prismatic beams under various static loading scenarios. The experimental strains required for the iFEM reconstruction are obtained from a high fidelity FE model of the beam modeled in ABAQUS. The solid beam geometries are meshed using the C3D8R element, an 8-node linear brick element with reduced integration. The thin-walled beams are modeled as shell structures and are meshed using the S8R element, an 8-node thick shell element with reduced integration and a quadratic interpolation of displacements. The iFEM reconstruction accuracy is assessed by comparing it to the displacement results of the direct FE model. All beams geometries used have a length of 20 m, and the chord length of the airfoil profiles used is 1 m. The thin-walled beams have a shell thickness of 5 mm.

Two different 1D iFEM elements are used to perform the displacement reconstruction: 0^{th} and 1^{st} order inverse elements. The elements were developed by Gherlone et al. [13, 19] and have been discussed extensively previously, but is briefly described in this section. For each 0^{th} order element, the strain measures $\{e_1, e_4, e_5, e_6\}$ are a constant throughout the element while $\{e_2, e_3\}$ has a linear interpolation across the element. Hence, the element

requires knowledge of the sectional strains at two axial locations for each element. At each axial location being investigated, three sensor positions along the beam perimeter are used. Furthermore, at each sensor position, two linear strain measurements are used, one along the axis to measure the axial strain and the second at an angle, β (usually 45^0), with respect to the beam axis to measure the shear strain, following the requirements of Equations 15. Therefore, a total of 12 experimental strain measurements are required per element. For the 1^{st} order element, strain measures $\{e_1, e_6\}$ are a constant, $\{e_4, e_5\}$ are linear and $\{e_2, e_3\}$ have parabolic interpolation across the element. So the element requires knowledge of the sectional strains at three axial locations and 18 experimental strain measurements per element.

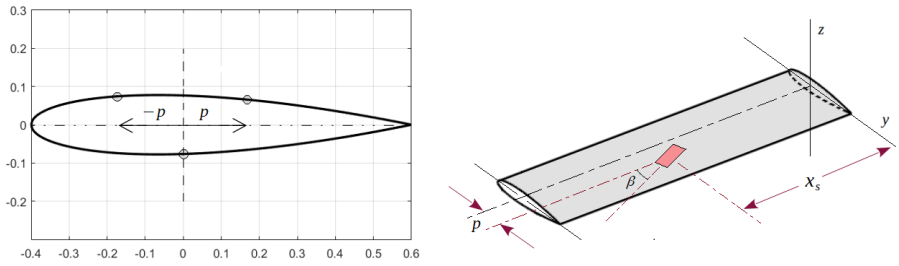


Figure 6: Parametrical representation of the sensor positions as a function of the chord length(left); The parameters, $[p, x_s, \beta]$, used to represent the sensor position and orientation for a strain gauge placed on the upper surface of the beam (right)

A simple convention is proposed to accurately describe the position and orientation of a sensor at any location on the surface of the beam regardless

of the airfoil profile: $[p^{\pm}, x_s, \beta]$, where the variable, p, indicates the position of a sensor on the surface of the beam, with respect to the centroid of the section, and is measured as the distance along the chord line of the airfoil profile. It is parameterized with respect to the airfoil chord length to get a normalized distance value for any profile. The superscript indicates whether the sensor is positioned on the beam's top or bottom surface, respectively. The variables x_s and β denote the length along the centroidal axis from the root and the orientation of the sensor with respect to the centroidal axis, respectively. A simple representation of the parameters is shown in Figure 6. So, for a sensor located 10% of the chord length from the centroid, placed on the upper surface and is one-third of the beam length, L, from the root and oriented at an angle of 60^0 with respect to the centroidal axis, the notation would be $\left[0.1^+, \frac{L}{3}, 60\right]$. This particular sensor position and arrangement can be visualized by referring to Figure 7.

4.1. Optimal Strain Sensor Placement

Finding the optimal location for placing the strain gauges on the surface of the beam is an aspect which influences the results of the iFEM solution. When choosing the sensor location, the objective is to maximize the quantity and quality of strain information available in any section. In this context, it

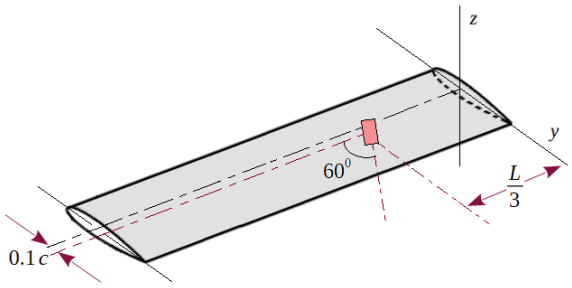


Figure 7: A strain sensor placed on the upper side of the beam, whose position and orientation conforms to the notation $\left[0.1^+, \frac{L}{3}, 60\right]$

may seem obvious that two sensors placed too close-by or too far apart may not provide the desired strain information. An iterative study is performed to gain a quantitative measure of the optimal sensor location for a symmetric airfoil profile [21].

The parameter being iterated is the variable, p, defined previously. Three strain sensor positions are required at each axial location of the beam, and a sensor configuration that is symmetric with respect to the centroid of the beam is desired. A solid cantilevered prismatic beam with a NACA 0016 airfoil profile, with unit tip forces applied along the two transverse axes, is used as the model for the study, and a high fidelity FE model is used to obtain the input strains and reference displacements. One 0^{th}-order beam element is used for the iFEM reconstruction and the sensor configuration

used can be described as: $\big[(\pm p^{+}, 0^{-}), (\frac{L}{3}, \frac{2L}{3}), (0, 45)\big]$. For each iterated sensor configuration, the beam tip displacements are reconstructed, and the percentage error in the displacements are calculated using Equation 22.

$$\%Error_U = \Big(\frac{U_{tip}^{FEM} - U_{tip}^{iFEM}}{U_{tip}^{FEM}}\Big) X100, \quad U = \{u, v, w, \theta_x, \theta_y, \theta_z\} \tag{22}$$

Only the percentage error in the axial displacement, u, and the two transverse displacements,$\{v, w\}$, are used for the optimal sensor placement effort. The results of the rotational displacements are ignored. For a suitable comparison between the absolute error values for all three displacements, the results are further normalized using Equation 23 so that they lie within the range of $(0, 1)$. The absolute and normalized percentage error values are plotted in Figure 8.

$$Normalized\ \%Error_U = \Big(\frac{\%Error_U - \%Error_{U,min}}{\%Error_{U,max} - \%Error_{U,min}}\Big) \tag{23}$$

The results of the iterative study show that percentage error increases for u and v and decreases for w, the further a sensor is positioned from the centroid. The absolute value of percentage errors shows that the magnitude of the

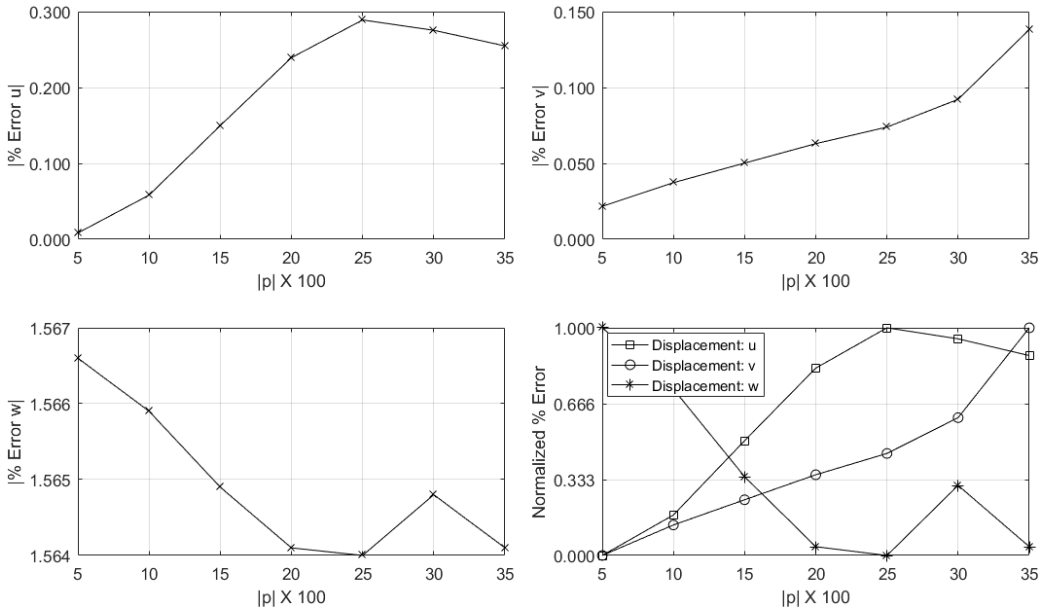


Figure 8: Absolute and normalized percentage error plots of beam tip displacements, u, v and w, plotted as a function of the sensor position p

errors are low, $< 1\%$ for u, v, and $< 2\%$ for w, highlighting the high accuracy of the results. The absolute values also illustrate the higher sensitivity of displacements u and v with varying sensor positions compared to w. For selecting a suitable sensor position, the plot of the normalized percentage error is used. A suitable sensor position would be one that presented a minimum in all the three tip displacement errors. Based on the results of Figure 8, a position approximately 10-20 % of the chord length from the centroid seems suitable. The theoretical formulation of the iFEM does not influence the choice of axial position for the sensors. It is only influenced by

practical considerations such as any unwanted strain fields due to the effect of the free end or constraints present at the root. Hence, axial locations sufficiently far from the root or the tip and from each other would be ideal.

4.2. Tip Loading Cases

The performance of the new iFEM formulation is tested using the example problem of a solid prismatic beam with a cambered airfoil profile (NACA 6516). The beam is subjected to a generalized tip load consisting of axial, transverse concentrated loads, out-of-plane moments, and torsion applied at the centroid of the beam (see Figure 9). The magnitude of the forces is $1N$ and the moments and torsion are $1Nm$.

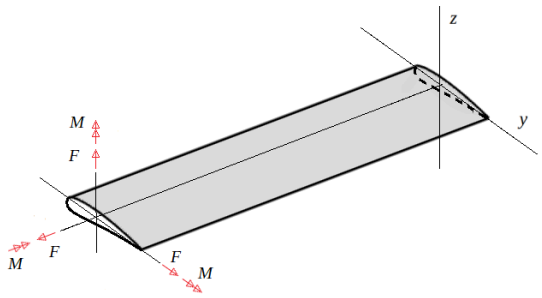


Figure 9: Generalized tip load on a solid prismatic beam with a NACA 6516 airfoil profile $[F = 1N, M = 1Nm]$

One 0^{th}-order beam element is used for the displacement reconstruction, and the sensor configuration used is described in Table 4.The accuracy of

Table 4: Sensor position used for the 0^{th}-order beam element and the percentage error in tip displacements for the solid prismatic beam under a generalized tip load

Sensor Positions	u	v	w	θ_x	θ_y	θ_z
$\left[(\pm 0.1^+, 0^-), (\frac{L}{3}, \frac{2L}{3}), (0, 45)\right]$	0.93	-5.51	-0.53	-4.66	1.09	-5.59

the iFEM is assessed by comparing the reconstructed tip displacements and rotations to the reference results coming from the direct FE model using Equation 22.

The percentage error in tip displacements and rotations are shown in Table 4. The results present an interesting case where the magnitude of displacement in the two transverse directions will be different under similar loads due to the unsymmetrical nature of the beam profile. Due to greater moment of inertia about the $z-$axis than about the $y-$axis, ($I_{zz} > I_{yy}$), the displacement along the $z-$axis will be greater than along $y-$axis ($w > v$). This difference in the displacement field is also reflected in the strain data, causing a more accurate reconstruction of w than v. The reconstruction of the torsional rotation is also seen to be accurate, with an error of -4.66%. In previous works [21], as transverse shear strain due to torsion was erroneously considered a function of the distance from the shear center, the error in θ_x was found to be around 34%. So the present results provide validation to the improvements made in the formulation.

462 The current reconstruction results were obtained by using only one inverse element for the entire beam. Increasing the number of inverse elements
464 used (and correspondingly, the number of experimental strain measurements) along the beam axis would improve the reconstruction accuracy of the iFEM.
466 For the current problem, increasing the number of elements used is not essential as the results obtained using one element are accurate. As the main
468 focus of this paper is on extending the 1D-iFEM to beams with complex cross-sections, increasing the number of elements is not investigated further
470 in this paper. It is left for future works where more complicated beam structures will be investigated.

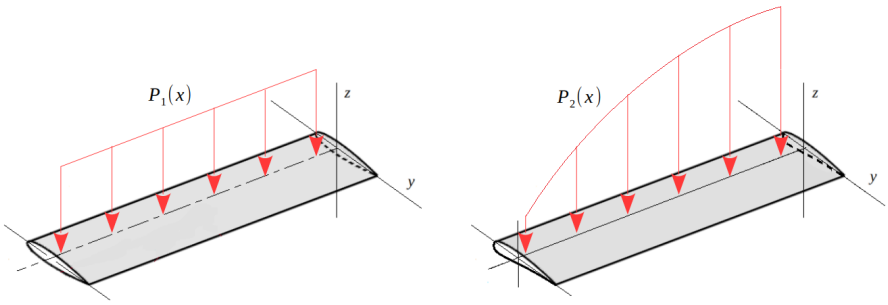


Figure 10: Uniform distributed load on a thin-walled prismatic beam with a NACA 0016 airfoil profile (left);non-uniform distributed load on a thin-walled prismatic beam with a NACA 6516 airfoil profile (right)

4.3. Distributed Loading Cases

The effect of a distributed load on the reconstruction results is tested with two prismatic, thin-walled (5mm thick), beams: one with a symmetric profile (NACA 0016) and the other with a cambered profile (NACA 6516). The former is subjected to a uniform distributed load, $P_1(x) = 1N/m$. The latter is subjected to a parabolic distributed load, made to resemble the aerodynamic loading experienced by an aircraft wing, with a greater load at the beam root, and it reduces and eventually vanishes at the beam tip (Figure 10). The distributed load is defined as a function of the centroidal axis and the beam length, L, as,

$$P_2(x) = \frac{1}{L^2}(L^2 - x^2) \qquad , 0 < x < L \tag{24}$$

For each load case, the displacement reconstruction results obtained using one 0^{th}-order beam element is compared to the results obtained using one 1^{st}-order beam element. According to the requirements of both elements, two different sensor distributions are also used (Table 5).

For the two distributed load cases, the reconstruction results of the displacement component, w, from both 0^{th} and 1^{st} order elements are normalized with respect to the tip displacement of the FE beam model and is plotted

Table 5: Sensor configurations used for the 0^{th} and 1^{st}-order beam elements in the case of a prismatic beam with distributed loading

Element Type	Number of Sensors	Sensor Location
0^{th} order	12	$\left[(\pm 0.2^{+}, 0^{-}), (\frac{L}{3}, \frac{2L}{3}), (0, 45)\right]$
1^{st} order	18	$\left[(\pm 0.2^{+}, 0^{-}), (\frac{L}{4}, \frac{2L}{4}, \frac{3L}{4}), (0, 45)\right]$

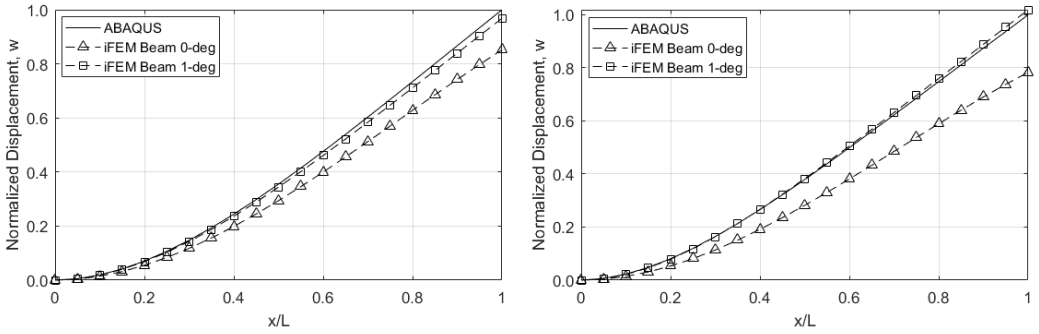


Figure 11: Plot of reconstructed normalized displacements using 0^{th} order and 1^{st} order inverse beam elements: uniform distributed load (left); parabolic distributed load (right)

in Figure 11. The percentage error in tip displacement, calculated using Equation 22, is shown in Table 6. It can be seen that the displacement reconstruction of the 1^{st} order element is less than 4% and improves significantly on that of the 0^{th} order element. As explained in the previous section, increasing the number of 0^{th} and 1^{st} order elements used for iFEM will improve the accuracy of the reconstructed displacements. However, the accuracy of the results when using the 1^{st} order element indicates that one element is sufficient, and further refinement is unnecessary. Structures with geometrical complexities that warrant further refinement will be addressed

Table 6: Percentage error in tip displacement,w, for the prismatic beams under distributed loading

Beam Profile	Load Condition	0^{th}-order	1^{st}-order
NACA 0016	Uniform Loading	-14.83	-3.15
NACA 6516	Parabolic Loading	-21.27	1.85

in future works.

In the present case, as the primary load was along the z-axis, the other two directions (x and y-axis) remain largely unloaded. Hence, the magnitude of the displacements $\{u, v\}$ are significantly smaller (by more than a factor of 10^{-3}). Hence, only the displacements in the loading direction have been analyzed.

5. Conclusion

This paper presented an improved framework for the 1D iFEM for handling geometrical complexities commonly encountered in the shape sensing of 3D aerospace structures. The effects of shear and torsion are important factors in describing the mechanical behavior of structures. This work presented the efforts in reconciling the 2D effects of shear and torsional strains with the assumptions of simple 1D beam theories. This was achieved with the help of certain shear coefficients and variation functions used to link the linear strain measured on the beam surface with an equivalent theoretical

transverse shear and torsional strain at any cross-section.

The performance of this new formulation was demonstrated through some example problems of prismatic beams under various static loading scenarios. The results of the iFEM show much greater reconstruction accuracy for torsional displacements compared to results from previous works, underlying the importance of the changes proposed in this work. Transverse displacement reconstruction of prismatic beams was also seen to be accurate under both uniform and non-uniform distributed loading, with greater accuracy seen to be obtained when using a higher-order inverse beam element.

Although the changes introduced in this paper offer a way of applying the 1D-iFEM for the shape sensing of a greater number of real-life aerospace structures, it can by no means account for all the geometrical complexities observed in real structures. Further refinement of the methodology is an essential part of existing research in this area. Future research aims to bridge this gap by focusing on thin-walled beam structures with additional stiffening elements such as ribs and spars and how they affect overall shape sensing behavior. As the current work focused primarily on prismatic beams, future work will emphasize beams with a tapered or variable profile along the beam length. Reconstruction performance under high and low-frequency structural

excitations will also be investigated.

Funding Acknowledgement

This research did not receive any specific grant from funding agencies in the public, commercial, or not-for-profit sectors.

References

[1] Gherlone, M., Mattone, M., Surace, C., Tassotti, A., Tessler, A. *Novel vibration-based methods for detecting delamination damage in composite plate and shell laminates*, Eng. Mat., Vol. 293–294, 289–296, 2005

[2] Corrado, N., Durrande, N., Gherlone, M., Hensman, J., Mattone, M., Surace, C. *Single and multiple crack localization in beam-like structures using a Gaussian process regression approach.* , J. Vib. Control, Vol. 24(18), 4160–4175, 2018

[3] Colombo, L., Sbarufatti, C., Giglio, M., *Definition of a load adaptive baseline by inverse finite element method for structural damage identification*, J. Mech. Syst. Signal Process., Vol. 120, 584–607, 2019

[4] Yan, B., Dai, P.,Liu, R.,Xing, M., Liu, S. *Adaptive super-twisting sliding*

mode control of variable sweep morphing aircraft, Aero. Sc. & Tech., Vol. 92,198-210, 2019

[5] Xu, D., Hui, Z.,Liu, Y.,Chen, G. *Morphing control of a new bionic morphing UAV with deep reinforcement learning,*, Aero. Sc. & Tech., Vol. 92, 232-243, 2019

[6] Jones, R.T., Bellemore, D.G., Berkoff, T.A., Sirkis, J.S., Davis, M.A., Putnam, M.A., Friebele, E.J., Kersey, A.D., *Determination of cantilever plate shapes using wavelength division multiplexed fiber Bragg grating sensors and a least-squares strain-fitting algorithm.*,Smart Mater. Struct., Vol. 7, 178–188, 1998

[7] Kang, L.H., Kim, D.K., Han, J.H., *Estimation of dynamic structural displacements using fiber Bragg grating strain sensors.*,J. Sound Vib., Vol. 305, 534–542, 2007

[8] Kim, N.S., Cho, N.S., *Estimating deflection of a simple beam model using fiber optic Bragg-grating sensors* , Exp. Mech., Vol. 44, 433–439, 2004

[9] Esposito, M., Gherlone, M., *Composite wing box deformed-shape reconstruction based on measured strains: Optimization and comparison of existing approaches* , Aero. Sc. & Tech., Vol. 99, 105758, 2020

[10] Ko, W.L., Richards, W.L., Fleischer, V.T., *Applications of the Ko displacement theory to the deformed shape predictions of the doubly-tapered Ikhana wing*, NASA/TP-2009-214652, 2009

[11] Tessler, A., Spangler, J.L. *A variational principle for reconstruction of elastic deformation of shear deformable plates and shells*, NASA TM-2003-212445, 2003

[12] Tessler, A., Spangler, J.L., *A least-squares variational method for full-field reconstruction of elastic deformations in shear-deformable plates and shells*, Methods Appl. M., Vol. 194, 327–339, 2005

[13] Gherlone, M.,Cerracchio, P., Mattone, M., Di Sciuva, M., Tessler, A., *Shape sensing of 3D frame structures using an inverse Finite Element Method*, Int. Journal of Solids and Structures, Vol. 49, Issue 22, 2012

[14] Tessler, A., Roy, R.,Esposito, M., Surace, C., Gherlone, M., *Shape Sensing of Plate and Shell Structures Undergoing Large Displacements using the inverse Finite Element Method*, Shock and Vibration, Vol. 2018, 8076085, 2018

[15] Vazquez, S.L., Tessler, A., Quach, C.C., Cooper, E.G., Parks, J., Span-

gler J.L., *Structural health monitoring using high-density fiber optic strain sensor and inverse finite element methods*, NASA TM-2005-213761, 2005

[16] Roy, R., Gherlone, M., Surace, C., *Damage localisation in thin plates using the inverse Finite Element Method*, In: Proceeding of 6th Damage Assessment of Structures, Porto, 2019.

[17] Zhao, Y., Du, J., Bao, H., Xu, Q. *Optimal Sensor Placement Based on Eigenvalues Analysis for Sensing Deformation of Wing Frame Using iFEM*, Sensors, Vol. 18(8), 2424, 2018; doi:10.3390/s18082424.

[18] Zhao, F., Bao, H., Xue, S., Xu, Q. *Multi-Objective Particle Swarm Optimization of Sensor Distribution Scheme with Consideration of the Accuracy and the Robustness for Deformation Reconstruction*, Sensors, Vol. 19(6), 1306, 2019; doi:10.3390/s19061306

[19] Gherlone, M., Cerracchio, P., Mattone, M., Di Sciuva, M., Tessler, A., *An inverse finite element method for beam shape sensing: theoretical framework and experimental validation*, Smart Mater. Struct., Vol. 23(4), 2014

[20] Zhao, F., Xu, L., Bao, H., Du, J. *Shape sensing of variable cross-section*

600 *beam using the inverse finite element method and isogeometric analysis*,
Measurement, Vol. 158, 107656, 2020; doi:10.1016/s20107656

602 [21] Roy, R., Gherlone, M., Surace, C., *Shape sensing of beams with complex
cross sections using the inverse Finite Element method*, In: Proceeding of
604 12th International Workshop on Structural Health Monitoring, Stanford,
CA., 2019.

606 [22] Timoshenko, S. P., and Goodier, J. N., *Theory of Elasticity*,3rd ed.,
McGraw–Hill, New York, 1970.

608 [23] C. Y. Wang, *Exact torsion solutions for certain airfoil shapes*, AIAA
Journal, Vol. 55, No. 12, 2017

610 [24] Kosmatka, J. B., *Flexure-Torsion Behavior of Prismatic Beams, Part
I: Section Properties via Power Series*, AIAA Journal, Vol. 31(1), 1993,
612 170–179; doi:10.2514/3.11334

[25] Carpinteri, A., *Structural Mechanics Fundamentals*, CRC Press, FL,
614 2013

[26] Serafini, J., Bernardini, G.,Porcelli, R.,Masarati, P. *In-flight health mon-*

616 *itoring of helicopter blades via differential analysis*, Aero. Sc. & Tech., Vol. 88, 436-443, 2019